processes

MDPI

Article

Simulation and Experimental Design of Magnetic Fluid Seal Safety Valve for Pressure Vessel

Zhenggui Li [1,2,*], Ziyue Wang [2,3,4], Changrong Shen [3], Wangxu Li [2], Yanxiong Jiao [1], Chuanshi Cheng [5], Jie Min [5] and Yuanyuan Li [5]

[1] School of Engineering, Qinghai Institute of Technology, Xining 810016, China
[2] Key Laboratory of Fluid and Power Machinery, Ministry of Education, Xihua University, Chengdu 610039, China
[3] Jiangsu Water Resources Co., Ltd., East Route of South-to-North Water Diversion, Nanjing 215341, China
[4] Sichuan Huadian Luding Hydropower Co., Ltd., Luding 610041, China
[5] China Yangtze Power Co., Ltd., Maintenance Plant, Yichang 443000, China
* Correspondence: lzhgui@mail.xhu.edu.cn

Abstract: This article focuses on the safety valve of pressure vessels, and a new ferrofluid sealing device for pressure vessel safety valves is developed based on a special magnetic circuit. A combined method of numerical calculation and experimental analysis is used to study the relationship between seal clearance, number of seals, pole slot width, pole tooth height, pole tooth width, and the sealing pressure of the ferrofluid sealing device. The research results show that seal clearance and pole tooth width have a significant impact on the sealing performance, and as the dimensions increase, the sealing pressure decreases. As the number of seals, pole tooth height, and slot width increase, the sealing performance initially improves and then decreases. This phenomenon is attributed to the increase in magnetic reluctance in the magnetic circuit. In experimental studies, when the excitation current of the electromagnet is 240 mA and the coil turns number 30, the sealing capacity is 61.22 kPa. When the excitation current is 200 mA and the coil turns number 80, the sealing capacity is 168.24 kPa. The experiments demonstrate the compensating ability of magnetic fluid seals in combination with safety valve seals, confirming that combined seals have higher reliability compared to conventional mechanical seals.

Keywords: pressure vessel safety valve; ferrofluid sealing device; polar tooth parameters; sealing capacity

Citation: Li, Z.; Wang, Z.; Shen, C.; Li, W.; Jiao, Y.; Cheng, C.; Min, J.; Li, Y. Simulation and Experimental Design of Magnetic Fluid Seal Safety Valve for Pressure Vessel. *Processes* **2024**, *12*, 2040. https://doi.org/10.3390/pr12092040

Academic Editors: Dimitris Ipsakis and Andreas Yiotis

Received: 4 September 2024
Revised: 17 September 2024
Accepted: 20 September 2024
Published: 21 September 2024

1. Introduction

Pressure vessels, as process equipment for storing and carrying high-pressure gases or liquids, play a significant role in the industrial field. The sealing performance of pressure vessels is crucial to the reliability, stability, and safety of energy systems. Therefore, there is widespread attention being paid to exploring long-term effective sealing methods [1–3]. Traditional sealing methods used in process equipment like pressure vessels, such as flange connections, threaded seals, and rubber seals, often struggle to achieve high reliability in sealing.

Issues such as the loosening of flange seals during prolonged operation, minute leaks due to imprecise machining of threaded seals, and deformations of rubber seals in corrosive environments make achieving reliable sealing challenging. Once these sealing problems occur, they can result in unnecessary economic losses, and even threaten human safety.

Ferrofluid is a new type of intelligent liquid that can control the shape of the magnetic fluid without contact using a magnetic field to achieve the desired effect. By guiding it into the sealing clearance, a liquid sealing ring can be formed. Compared to rubber seals and mechanical end-face seals, ferrofluid seals have better corrosion resistance and reliability. It has been reported that magnetic fluid seals in tank periscopes have a service life of

up to 10 years [4]. The excellent performance of ferrofluid seals has also been demonstrated in industrial products such as chemical equipment reactors [5], transportation equipment centrifugal pumps, and other applications [6]. With advancements in ferrofluid preparation processes and an understanding of the dynamic mechanism of ferrofluids, high-performance hydrophobic ferrofluid and high-temperature-resistant ferrofluids can now be mass-produced [7,8]. The theory of magnetic particle chaining under field conditions has been gradually accepted [9], the mechanisms of magnetic adhesion effects under magnetic and thermal fields have been revealed [10], and improvements have been made to the ferrofluid transport equations at small-micro-gap scales [11]. These new technologies and insights provide theoretical references for optimizing ferrofluid seals. However, under liquid environments or high-pressure conditions, ferrofluid seals still fall short of ideal performance. A new approach to resolving this issue involves combining ferrofluid seals with traditional seals in a combined sealing structure. For instance, Li [12] integrated ferrofluid with threaded seals in hydraulic equipment to achieve long-term effective dynamic sealing in liquid environments. Yang [13] proposed structural improvements by combining ferrofluid with labyrinth seals, using the groove part of the labyrinth seal as the magnetic assembly of the ferrofluid seal, significantly enhancing the pressure resistance of the ferrofluid seal. Wang [14] introduced an embedded ferrofluid seal combination structure based on mechanical end face seals, achieving tight leak-free sealing at 500 rpm and 0.5 MPa conditions. Other improvements combining general mechanical structures, such as adding grooved shafts [15] and buffer channels [16], have positively contributed to improving the stability of ferrofluid seal interfaces. For safety valve sealing, the drawbacks of traditional sealing forms have led to many potential hazards. Exploring new sealing methods has become an urgent technological challenge. With the development of the basic theory and application technology of ferrofluid seals, utilizing ferrofluid seals to supplement mechanical end face seals has emerged as a new approach to achieving the tight sealing of safety valves.

This article focuses on the research of ferrofluid seals for safety valves. It starts by selecting the type of ferrofluid based on high-temperature and high-pressure sealing environments. The stable mechanism of ferrofluids is analyzed from the perspectives of ferrofluid preparation and performance, considering thermodynamic parameters of ferrofluids to theoretically calculate pressure resistance. Subsequently, a coupling structure between mechanical end faces and ferrofluid seals is designed based on magnetic principles. Numerical methods are employed to study the impact of structural parameters on the performance of ferrofluid seals. Finally, experimental verification is conducted using a test rig for safety valve ferrofluid seals to confirm the feasibility and reliability of the seal structure. This study aims to provide technical guidance for addressing stability sealing issues in safety valves.

2. Preparation and Performance Analysis of Ferrofluids

The general temperature range that ferrofluids can withstand is between −20 °C and 105 °C; temperatures that are too high or too low can lead to the failure of the ferrofluid. According to investigations, the highest heat resistance values for ferrofluids based on diester, perfluoropolyether oil, and silicone oil carriers are 200 °C, 300 °C, and 350 °C, respectively. The safety valves developed in this study are mostly intended for high-temperature and high-pressure conditions. Although the temperature resistance values of perfluoropolyether oil and silicone oil are equally superior, perfluoropolyether oil is more expensive in terms of material cost. After comprehensive consideration, choosing silicone oil as the base fluid for preparing ferrofluids better meets production needs [17–21]. Chemical coprecipitation is a common method for synthesizing Fe_3O_4 nanoparticles. By applying chemical coprecipitation, the required magnetic particles can be rapidly obtained. The chemical reaction process is represented as $Fe^{2+} + 2Fe^{3+} + 8OH^- \rightarrow Fe_3O_4 + 4H_2O$. Taking 40.5 g of $FeCl_3 \cdot 6H_2O$ and 18.6 g of $FeCl_2 \cdot 7H_2O$, we dissolve them together in 250 mL of deionized water at 65 °C, then raise the temperature to 70 °C under constant

stirring. Next, we add 25.6 g of sodium hydroxide solution to the mixed solution while maintaining a stirring speed of 300 rpm, and continue stirring for 1 h to produce black Fe_3O_4 magnetic particles.

Subsequently, we maintain a constant reaction temperature of 50 °C using a water bath and slowly add hydrochloric acid in increments to the magnetic particles, adjusting the pH to the range of 4–5. We then add 90 mL of anhydrous ethanol and 6 mL of tetraethyl orthosilicate (TEOS) to the solution to initiate the hydrolysis and condensation reactions. Under continuous and uniform stirring, we let the mixture react for 1.5 h (hydrolysis process), and then gradually add sodium hydroxide solution during the reaction process to adjust the pH to 9–10 (condensation process) to ensure a thorough reaction progress. After completion, we place the solution in a magnetic field for separation. Firstly, we wash the separated material with anhydrous ethanol, followed by rinsing five to seven times with deionized water, to eventually obtain core–shell nano-magnetic particles of Fe_3O_4@SiO_2 (as shown in Figure 1a).

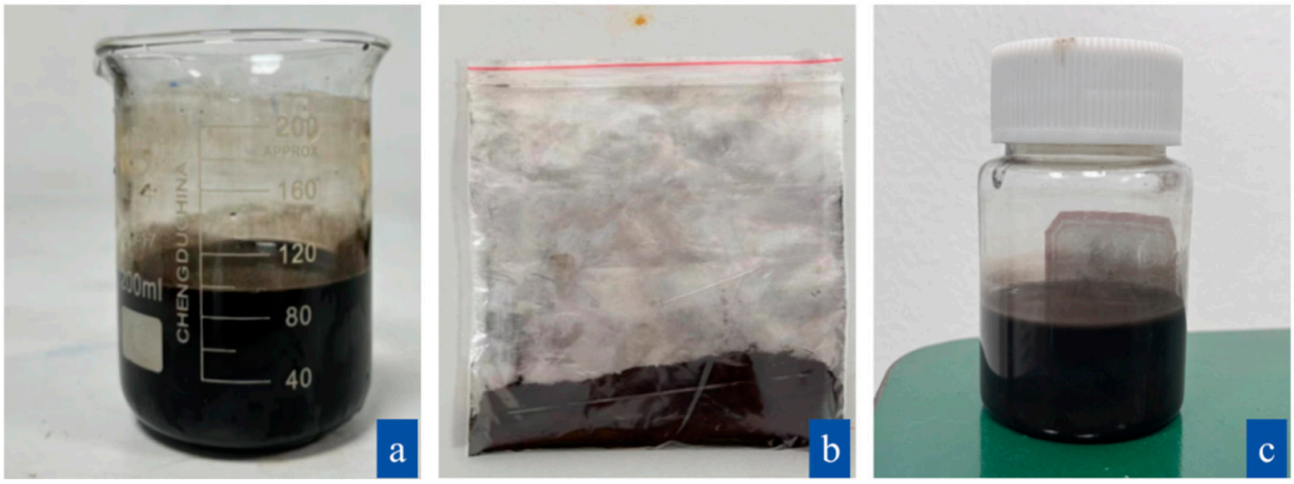

Figure 1. Samples of ferrofluid preparation process ((**a**) core–shell nano-magnetic particles; (**b**) dried nano-magnetic particles; (**c**) silicone-based ferrofluid).

We successively add 10 mL of deionized water, 10 mL of silane coupling agent A1120, and 180 mL of anhydrous ethanol, and gradually add hydrochloric acid to adjust the pH to the range of 4–5, stirring continuously for 2 h to ensure secondary coating on the Fe_3O_4@SiO_2. Upon completion of the secondary coating, we wash the sample three to five times with anhydrous ethanol and deionized water, then dry the sample at 80 °C for 12 h. Finally, we grind the sample, pack it, and store it to obtain dried Fe_3O_4@SiO_2@A1120 particles (Figure 1b).

According to reference materials [22], the magnetic particles are mixed with the base carrier liquid in a ratio of 1:3 (10 g of coated particles to 30 g of dimethyl silicone oil) at a temperature of 70 °C. We then stir uniformly at a mechanical stirring speed of 500 rpm for 2 h to ensure the even dispersion of the magnetic particles in the base liquid. After removing the undissolved large particles, a clear upper liquid is obtained, which is the stably dispersed silicone-based ferrofluid (Figure 1c). The hydrolysis and condensation processes of tetraethyl orthosilicate are depicted in Figure 2.

The crystalline structures of Fe_3O_4, Fe_3O_4@SiO_2, and Fe_3O_4@SiO_2@A120 particles were analyzed using the X-ray diffractometer Ultima IV (Rigaku Corporation, Tokyo, Japan), as shown in Figure 3. The consistency in diffraction peak positions indicates that the particle coating behavior does not alter the crystal structure of Fe_3O_4. Fourier transform infrared spectroscopy analysis of surface-treated nano-magnetic particles was conducted using the Nicolet iS20 Fourier Transform Infrared Spectrometer (Thermo Scientific, Waltham, MA, USA).

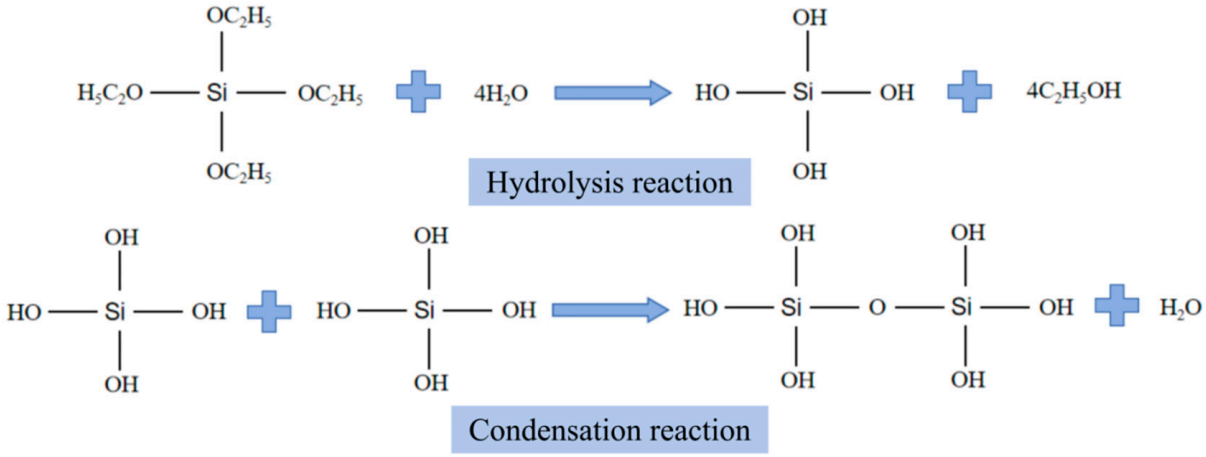

Figure 2. Hydrolysis and polycondensation of ethyl orthosilicate.

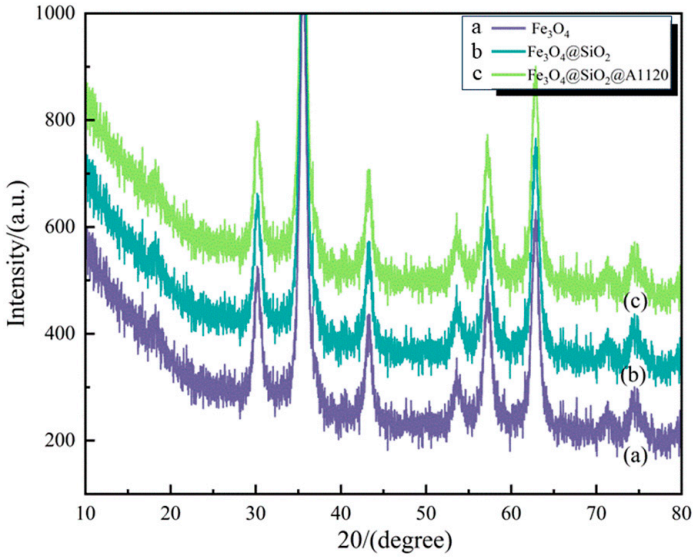

Figure 3. XRD of Fe_3O_4@SiO_2@A1120 nanoparticles.

Figure 4 presents the infrared spectra of Fe_3O_4@SiO_2 particles (a) and Fe_3O_4@SiO_2@A1120 particles (b). The data reveal two peaks corresponding to Si–O bonds at 1117.86 cm^{-1} and 1032.18 cm^{-1} on curve b, with additional peaks such as 1204.68 cm^{-1} corresponding to C-N stretching vibrations and 1449.57 cm^{-1} corresponding to C-H bending vibrations, matching the characteristic peaks of A1120. On curve a, only one peak corresponding to a Si–O bond is observed at 1018.67 cm^{-1}, along with characteristic hydroxyl group peaks at 1625.94 cm^{-1} and 1621.05 cm^{-1}.

The thermogravimetric analysis (TGA) of surfactant-modified particles was performed using the Mettler TGA2 Thermal Analyzer (Zurich, Switzerland), generating the weight loss curve depicted in Figure 5. It is observed that before 160 °C, the mass reduction of the particles primarily results from the evaporation of residual water attached to the surface of nanoparticles. As the temperature increases further, the decrease in thermal weight curve occurs due to the decomposition and evaporation of the surfactant enveloping the particle's surface. Additionally, within a temperature range of room temperature to 600 °C, Fe_3O_4@SiO_2@A1120 particles exhibit a weight loss 6.4% higher than that of Fe_3O_4@SiO_2 particles, confirming the successful encapsulation of A1120 on the surface of Fe_3O_4@SiO_2 particles.

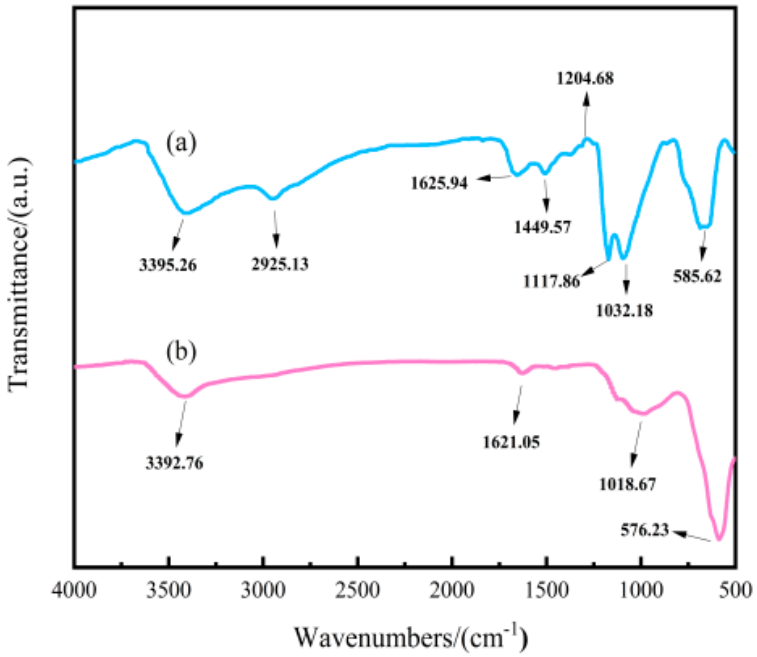

Figure 4. Infrared spectrum of Fe_3O_4@SiO_2@A1120 nanoparticles.

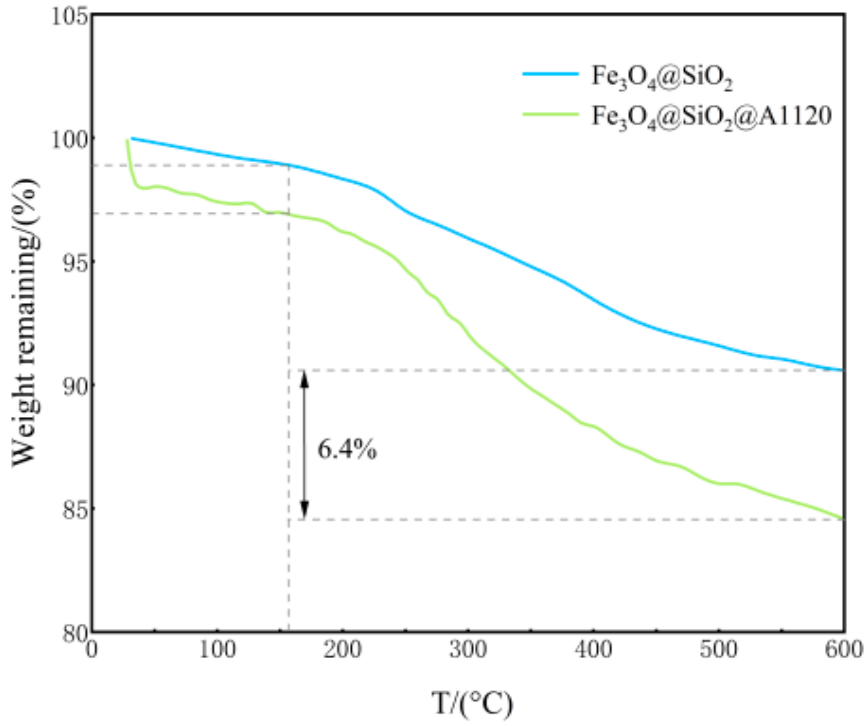

Figure 5. TG diagram of Fe_3O_4@SiO_2@A1120 nanoparticles.

Finally, after allowing the silicone-based ferrofluid to stand undisturbed in a gravitational field for 1 to 4 weeks, it was observed that the magnetic particles maintained a stable dispersed state with the base carrier liquid, without any signs of separation (Figure 6). In conclusion, the silicone-based ferrofluid prepared by chemical coprecipitation exhibits good stability and heat resistance.

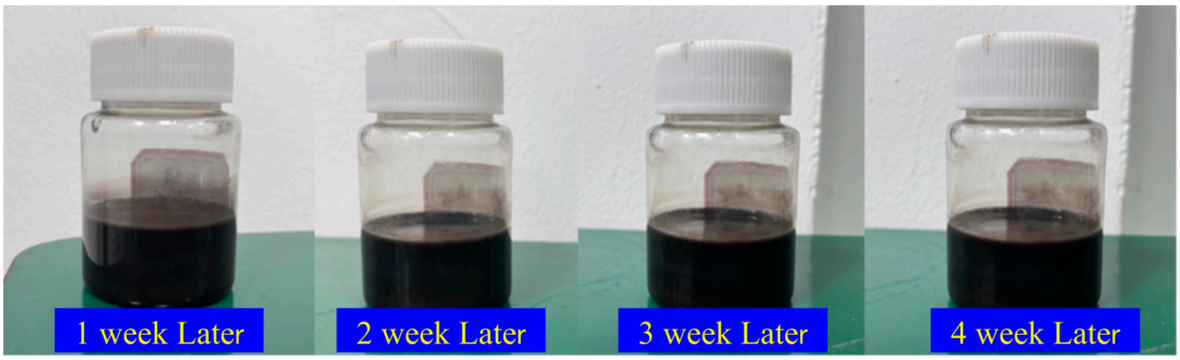

Figure 6. A static diagram of a silicone oil-based ferrofluid over a period of time.

3. Theoretical Analysis

Under the magnetic field environment, the ferrofluid present in the clearance forms a liquid sealing ring, as shown in Figure 7. The Bernoulli equation for ferrofluids derived from the general fluid Navier–Stokes equations is presented as Equation (1) [23–25]. Solving the physical problem depicted in Figure 7 yields the following: in a static seal configuration where the motion velocity v of the ferrofluid is 0 and the sealing medium and ferrofluid are at the same horizontal level, the relative elevation h is 0. Consequently, the expression for the maximum pressure Δp_{max} in the ferrofluid seal is obtained as given in Equation (2), where the minimum value of magnetic field intensity H_{min} in the seal clearance approaches 0, simplifying Equation (2) to Equation (3). In a multi-stage sealing device, the total sealing pressure is the sum of the individual single-stage sealing pressures, expressed as in Equation (4) [26–28].

$$p + \frac{1}{2}\rho v^2 + \rho g h - \mu_0 \int_0^H M dH = C \tag{1}$$

$$\Delta p_{max} = \mu_0 \int_{H_1}^{H_2} M dH \tag{2}$$

$$\Delta p_{max} = \mu_0 M_s H_{max} \tag{3}$$

$$\Delta p_{max} = N \mu_0 M_s H_{max} \tag{4}$$

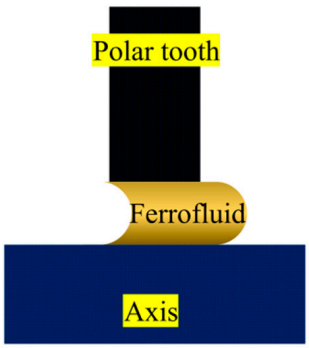

Figure 7. Distribution of magnetic liquid in the seal gap under static pressure seal.

In the equations, p represents fluid pressure, ρ indicates fluid density, g is the gravitational acceleration, μ_0 stands for the relative magnetic permeability of the ferrofluid, M denotes the magnetization intensity of the ferrofluid, M_s is the saturation magnetization intensity of the ferrofluid, H represents magnetic field intensity, H_{max} and H_{min} denote the maximum and minimum values of magnetic field intensity, and N signifies the number of sealing stages.

The transport equation for magnetic fluid in the gap is derived from Newton's second law. Ferrofluids working inside a safety valve must satisfy the Navier–Stokes (N-S) equa-

tions for ferrofluids. The significant difference between the N-S equations for ferrofluids and those for conventional fluids lies in the inclusion of the magnetic body force μ_0MH as a source term (Equations (5)–(7)).

$$\frac{\partial \mu_0 MH}{\partial x} - \frac{1}{\rho}\left(\frac{\partial p}{\partial x}\right) + \eta \nabla^2 v_x = \frac{\mathrm{d}v_x}{\mathrm{d}t} \tag{5}$$

$$\frac{\partial \mu_0 MH}{\partial y} - \frac{1}{\rho}\left(\frac{\partial p}{\partial y}\right) + \eta \nabla^2 v_y = \frac{\mathrm{d}v_y}{\mathrm{d}t} \tag{6}$$

$$\frac{\partial \mu_0 MH}{\partial z} - \frac{1}{\rho}\left(\frac{\partial p}{\partial z}\right) + \eta \nabla^2 v_z = \frac{\mathrm{d}v_z}{\mathrm{d}t} \tag{7}$$

where v_x, v_y and v_z are the velocity components in the x, y, and z directions, and η is the kinematic viscosity of the ferrofluid.

4. Numerical Model

The sealing structure of a safety valve generally employs a mechanical end face seal, as depicted in Figure 8a. The sealing performance deteriorates rapidly when the end face exhibits wear or unevenness. Leveraging the adsorption and flow characteristics of ferrofluids under the influence of a magnetic field, a magnetic circuit structure is designed to effectively distribute the ferrofluid uniformly in the gap between two contacting planes. As illustrated in Figure 8b, the upper part of the mechanical seal end face is designed with a polar tooth structure that perfectly fits the lower end face. With the application of a magnetic field, the polar teeth exhibit magnetization, creating a magnetic field gradient on the sealing end face, thus forming a ferrofluid seal structure. The magnetic field is supplied by an electromagnet; when the circuit is connected, the electromagnet acts as a magnetic source, generating a magnetic field based on the principle of electromagnetic induction. The magnetic field lines will extend along high-permeability materials, following Kirchhoff's magnetic circuit law. The variation in cross-sectional area of the polar tooth structure causes a sharp increase in magnetic induction intensity.

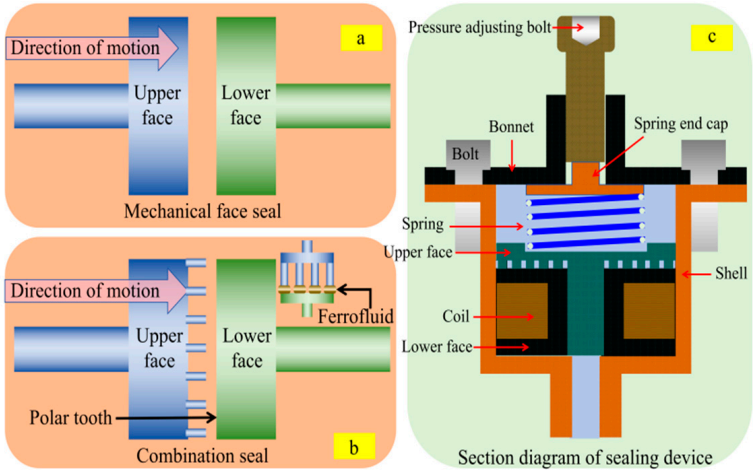

Figure 8. Ferrofluid seal safety valve model diagram ((**a**) mechanical seal concept diagram; (**b**) composite seal concept diagram; (**c**) section diagram of sealing structure).

Iron magnetic particles within the ferrofluid, possessing permanent magnetic dipole moments, react to the external magnetic field, aligning in chains and being fixed in the gap by magnetic forces, forming a liquid "O" ring seal. This effectively isolates the internal medium of the pipeline from the external environment. In the absence of a magnetic field, high-pressure gas enters the pipeline at high temperatures. Once the pressure exceeds the set pressure, the sealing end face is pushed off the electromagnet seat by the medium, resulting in seal failure. With the presence of a magnetic field, the sealing ability of the

safety valve comprises both the end face seal and the ferrofluid seal. This dual approach offers an improvement in sealing capability. Additionally, when the mechanical seal end face is not smooth, the ferrofluid can fill all gaps, blocking the passage, thereby achieving a seal. Consequently, there is an enhancement in the reliability and stability of the safety valve seal. Figure 8c illustrates the overall structure of the combined seal.

Using the finite element analysis software ANSYS Maxwell 16.0, numerical calculations are conducted on the ferrofluid sealing device under different seal clearances (l_x), numbers of sealing stages (n), polar tooth groove widths (l_s), polar tooth heights (l_h), and polar tooth widths (l_l). The axially symmetric structure of the ferrofluid sealing device allows for simplification using a two-dimensional model in numerical simulations. According to the requirements of small-pressure equipment safety valves (rated pressure < 0.8 MPa), a ferrofluid seal design for the safety valve is developed.

The ferrofluid seal structure comprises an electromagnet, a sealing top cover, a sealing bottom end, and the ferrofluid, as shown in Figure 9. In the numerical model, the electromagnet is constructed with a copper material, while the sealing top cover and polar teeth are made of 45# steel. The ferrofluid is composed of custom materials with a density of 1.279 g/cm^3, a saturation magnetization intensity of 281.1242 Gs, a thermal conductivity of 0.2 W/(m·K), and a relative magnetic permeability of 1.05. Boundary conditions for the model are set to Balloon (zero magnetic field at infinity, magnetic field tangential to boundaries but allowed to pass through).

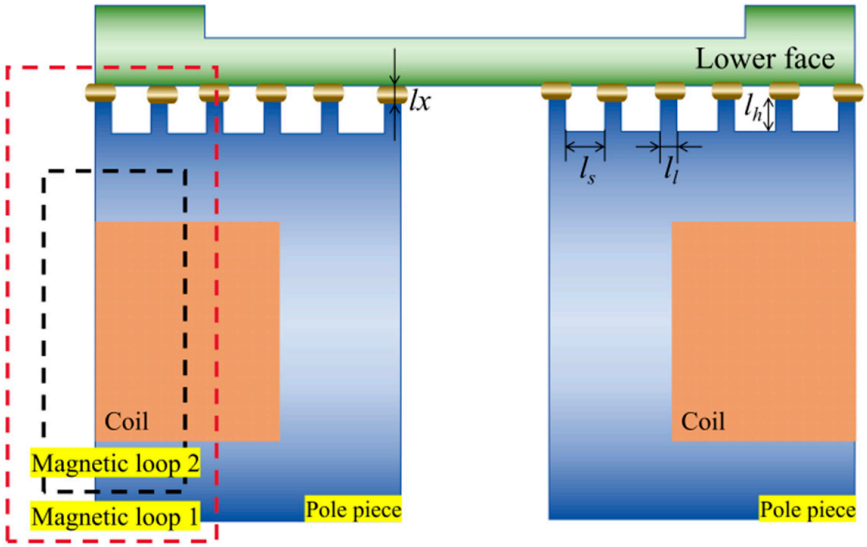

Figure 9. Structural diagram of the magnetic fluid seal part of the safety valve device.

The air domain size is set to 100% of the overall model. The radial bisector line between the sealing top cover and polar teeth is chosen as the study object. By exporting the data obtained from numerical simulations of the magnetic fluid sealing device under various seal clearances, sealing stages, polar tooth heights, polar tooth widths, and polar tooth groove widths, maximum magnetic induction intensity values are derived, then used to calculate the numerical sealing pressure.

The ferrofluid sealing system consists of two magnetic circuits. In the primary magnetic circuit, the magnetic lines generated by the coil start from the north (N) pole, successively passing through the magnetic poles, gaps, sealing top cover, air, and another magnetic pole, before returning to the south (S) pole. In the secondary magnetic circuit, the magnetic lines start from the north pole, pass through a magnetic pole, the outer air, and another magnetic pole, then return to the south pole, forming magnetic leakage on the outside of the device.

5. Result Analysis

5.1. Effect of Sealing Gap on Sealing Pressure

To investigate the relationship between seal clearances and the ferrofluid sealing safety valve device, this section sets the number of sealing stages as five, the polar tooth groove width as 2.0 mm, the polar tooth height as 2.0 mm, and the polar tooth width as 1.0 mm. Within the range of 0.1–0.5 mm, with a variation gradient of 0.1 mm, the study explores the relationship between seal clearances and magnetic sealing pressure. Magnetic field maps of the sealing devices under different clearance conditions are shown in Figure 10.

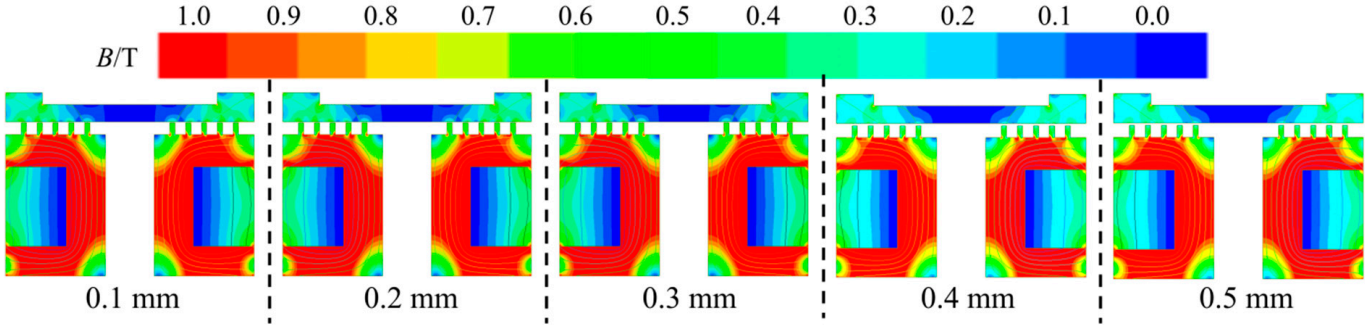

Figure 10. Cloud map of magnetic field distribution of sealing device at different gaps.

The key to the ferrofluid sealing device lies in the effect of the gap magnetic field, where the sealing performance is directly related to the magnetic field gradient. The greater the magnetic field gradient, the better the sealing performance. Therefore, it is crucial to delve into the region of the magnetic field within the gap.

Figure 11 shows Magnetic induction intensity of cut-off line under different seal gap conditions. With an increase in the seal clearance, the air's magnetic reluctance in the magnetic circuit increases. As a result, the positive peak value of the magnetic induction intensity gradually decreases while the negative peak value increases. For example, at gap values of 0.1 mm and 0.5 mm, the positive peak value decreases from 0.3896 T to 0.2291 T, and the negative peak value increases from 0.0387 T to 0.101 T.

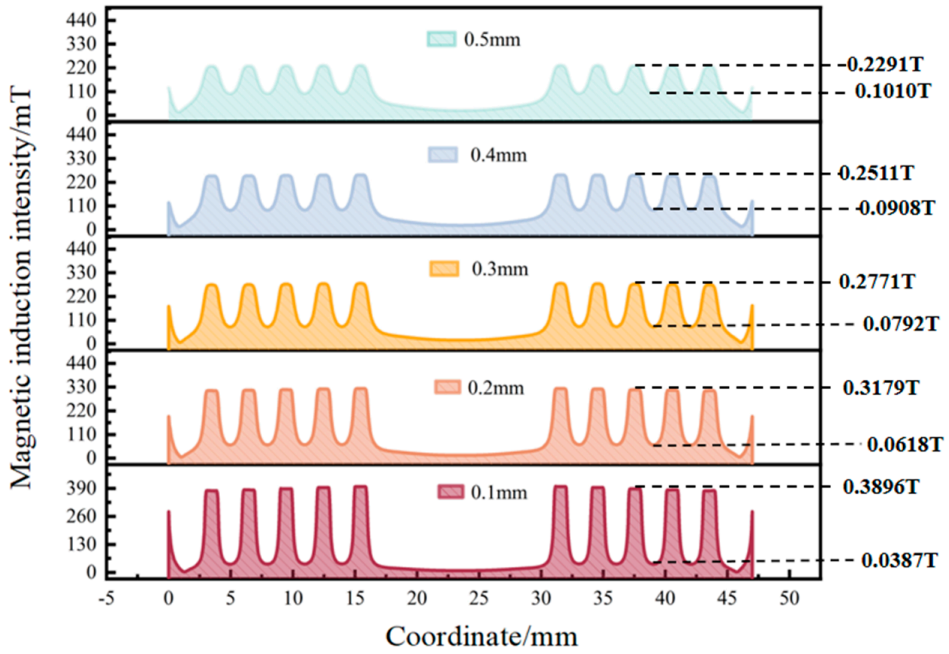

Figure 11. Magnetic induction intensity of cut-off line under different seal gap conditions.

By calculating the difference between the positive and negative peak values shown in Figure 8 to obtain the magnetic induction intensity gradient, and combining it with the sealing pressure formula, it can be inferred that the sealing capability is 35.12 kPa, 30.74 kPa, 23.75 kPa, 19.24 kPa, and 15.38 kPa for seal clearances ranging from 0.1 mm to 0.5 mm. The fundamental reason for the decrease in sealing capability lies in the increased magnetic reluctance at the seal clearance, leading to a reduction in the binding force of the ferrofluid. This manifests in the physical quantities of magnetic induction intensity as a decrease in the positive peak value, an increase in the negative peak value, and a reduction in the magnetic induction intensity gradient.

5.2. Effect of Sealing Stage on Sealing Pressure

Since the ferrofluid seal mainly acts as a compensatory seal in the safety valve device, with the primary sealing of high-pressure gas relying on mechanical seals, this section sets the number of polar teeth in the range of one to seven based on existing research results. The seal clearance is constrained to 0.1 mm, the polar tooth groove width is 2.0 mm, the polar tooth height is 2.0 mm, and the polar tooth width is 1.0 mm. With an increment of one in the number of stages, the relationship between the number of sealing stages and magnetic sealing pressure is studied. Magnetic field maps of the sealing devices under different numbers of sealing stages are shown in Figure 12.

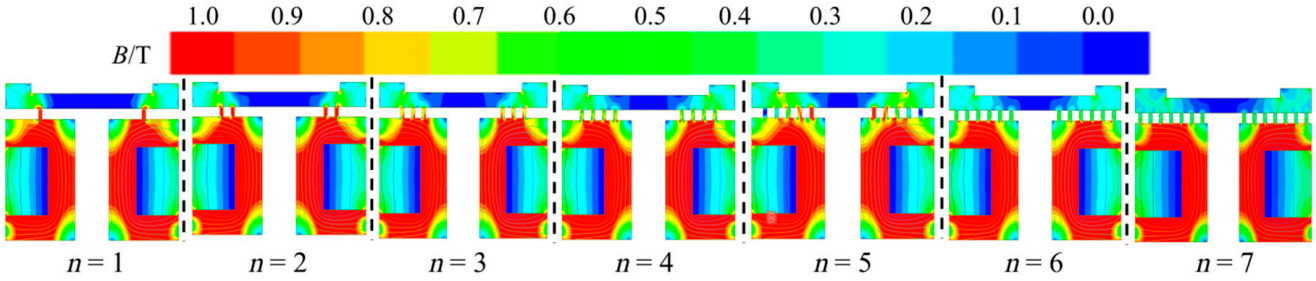

Figure 12. Cloud map of magnetic induction intensity distribution at different sealing stages.

When the number of stages is one, the magnetic induction intensity at the polar teeth portion exceeds 1 T. With more than three stages, the presence of multiple polar teeth generates additional magnetic circuits, each containing air magnetic reluctance, leading to increased magnetic losses and a subsequent decrease in the magnetic induction intensity at the polar teeth portion. However, when considering sealing capability, it is essential to comprehensively evaluate the impact of both the number of stages and the magnetic induction intensity gradient.

Figure 13 shows the distribution curves of magnetic induction intensity at the top and bottom center of the polar teeth. As the number of stages increases, both the positive and negative peak values of the magnetic induction intensity at the seal clearance gradually decrease. The positive peak values for n = 1 and n = 7 are 1.2897 T and 0.2777 T, while the negative peak values are 0.0923 T and 0.0282 T, respectively. The decrease in positive peak value is detrimental to overall sealing performance improvement, whereas the decrease in negative peak value is beneficial for enhancing overall sealing performance. The effects of these two values are opposite, but the positive peak value changes more rapidly. Overall, the magnetic induction intensity gradient at the seal clearance shows a decreasing trend.

Although the magnetic induction intensity of an individual polar tooth decreases with an increase in the number of stages, the sealing pressure of a multi-stage seal is related to the sum of the magnetic induction intensity gradients of all polar teeth. By summing up the sealing capabilities of each stage, as shown in Figure 14, the comprehensive sealing performance improves with an increase in the number of stages. For example, the sealing pressure is 23.96 kPa for n = 1 and 35.12 kPa for n = 5. However, blindly increasing the number of stages without considering the total magnetic potential does not consistently enhance sealing performance. Additional stages introduce more magnetic reluctance,

including material reluctance and air gap reluctance, leading to a decrease in total sealing capability. For instance, the sealing capability is 35.53 kPa at n = 6 and 34.94 kPa at n = 7. This result indicates that the optimal number of sealing stages for the designed ferrofluid seal safety valve in this study is 6.

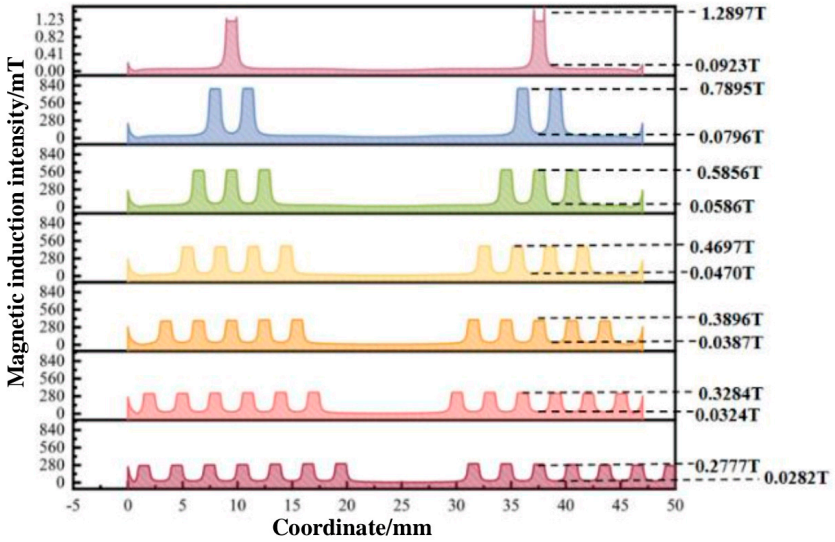

Figure 13. Magnetic induction intensity of truncated line under different sealing stages.

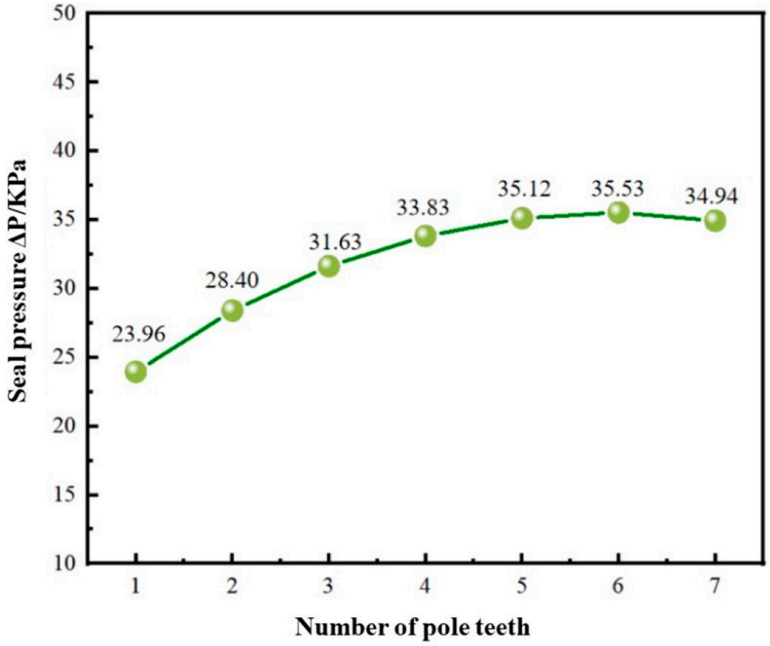

Figure 14. Seal pressure diagram under different seal clearance values.

5.3. Effect of Slot Width on Sealing Pressure

To investigate the relationship between groove width and the ferrofluid seal safety valve device, variables are strictly controlled. The parameters include a seal clearance of 0.1 mm, six polar teeth, a polar tooth height of 2.0 mm, and a polar tooth width of 1.0 mm. The groove is the space between the polar teeth, where a single-stage seal has no grooves, and in a multi-stage seal, the number of grooves is n-1. In this numerical simulation with six polar teeth, there are five grooves. This section sets the groove width in the range of 0.5–2.5 mm with a gradient of 0.5 mm to study the relationship between seal clearance and sealing pressure. Magnetic field maps of the sealing devices under different groove widths are shown in Figure 15.

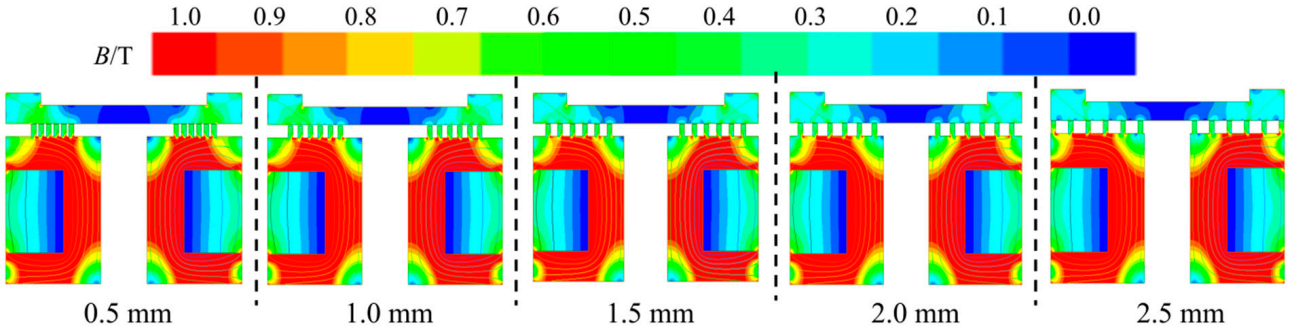

Figure 15. Magnetic field cloud image of a sealing device with different slot widths.

Increasing the groove width does not significantly alter the distribution pattern of the magnetic field. According to the magnetic induction distribution curves at the seal clearance (Figure 16), it is evident that the influence of groove width on the positive peak value of the magnetic induction intensity is relatively small. For groove widths of 0.5 mm and 2.5 mm, the positive peak values are 0.3539 T and 0.3183 T, respectively, showing a slight decrease with increasing groove width. Furthermore, with larger groove widths, there is less mutual influence between the polar teeth, weakening the leakage flux at the roots of the polar teeth and leading to a reduction in the negative peak value of the magnetic induction intensity. At groove widths of 0.5 mm and 2.5 mm, the negative peak values are 0.1262 T and 0.0257 T, respectively.

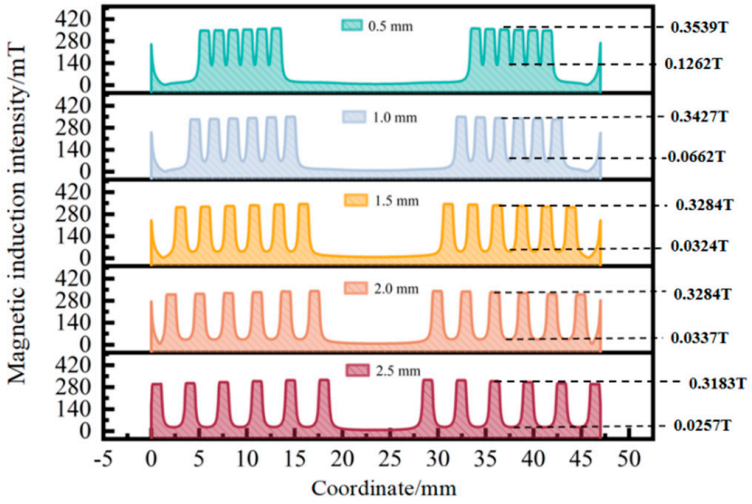

Figure 16. Magnetic induction intensity at different slot widths.

Calculations of the sealing performance at different groove widths yield sealing capabilities of 27.33 kPa, 33.19 kPa, 35.53 kPa, 35.37 kPa, and 35.12 kPa for groove widths of 0.5, 1.0, 1.5, 2.0, and 2.5 mm, respectively. The optimal sealing performance occurs at a groove width of 1.5 mm.

5.4. Influence of Pole Tooth Height on Sealing Pressure

Setting the seal clearance to 0.1 mm, with six polar teeth, a groove width of 1.5 mm, and a polar tooth width of 1.0 mm, this study explores the relationship between polar tooth height and the ferrofluid seal safety valve device. By incrementing in steps of 0.5 mm, the magnetic field and sealing performance are investigated for polar tooth heights ranging from 0.5 to 3.0 mm. Figure 17 displays the magnetic induction intensity distribution maps for different polar tooth heights.

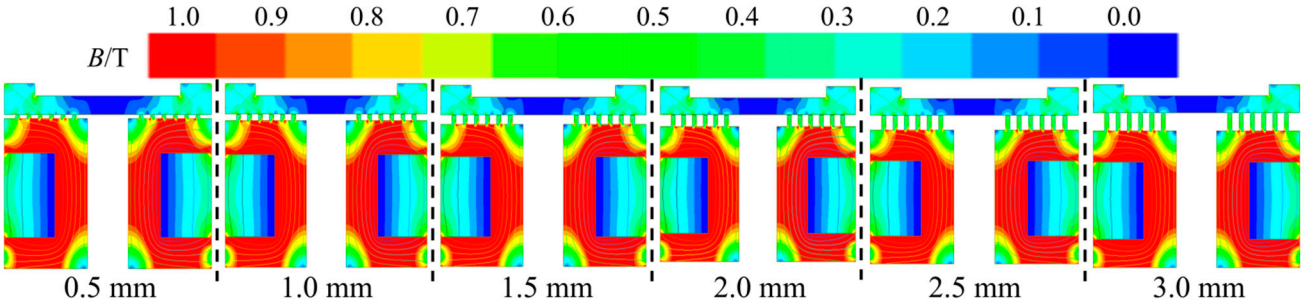

Figure 17. Magnetic field cloud image of the sealing device under different pole tooth heights.

Increasing the polar tooth height accentuates the geometric differences between the polar teeth and the top surface, facilitating the better transmission of magnetic induction along the polar teeth, thereby reducing leakage flux at the ends of the polar teeth and enhancing magnetic aggregation capabilities. When analyzing the magnetic induction intensity distribution curve at the clearance (Figure 18), it is observed that as the polar tooth height increases, the positive peak value initially increases and then decreases, while the negative peak value first decreases and then increases. Overall, there is a trend of the magnetic induction intensity gradient initially increasing with polar tooth height, and then decreasing. For polar tooth heights of 0.5, 1.0, 1.5, 2.0, 2.5, and 3.0 mm, the sealing capabilities are 30.91 kPa, 34.61 kPa, 35.22 kPa, 35.53 kPa, 35.37 kPa, and 35.19 kPa, respectively. The optimal sealing performance is achieved at a polar tooth height of 2.0 mm. The fundamental reason for the improvement in sealing performance with increased polar tooth height is the enhancement in the magnetic aggregation ability. Once the sealing performance reaches its maximum, it indicates efficient utilization of the magnetic potential. Further increasing the polar tooth height introduces additional material (polar teeth) reluctance, leading to a slight decline in sealing performance.

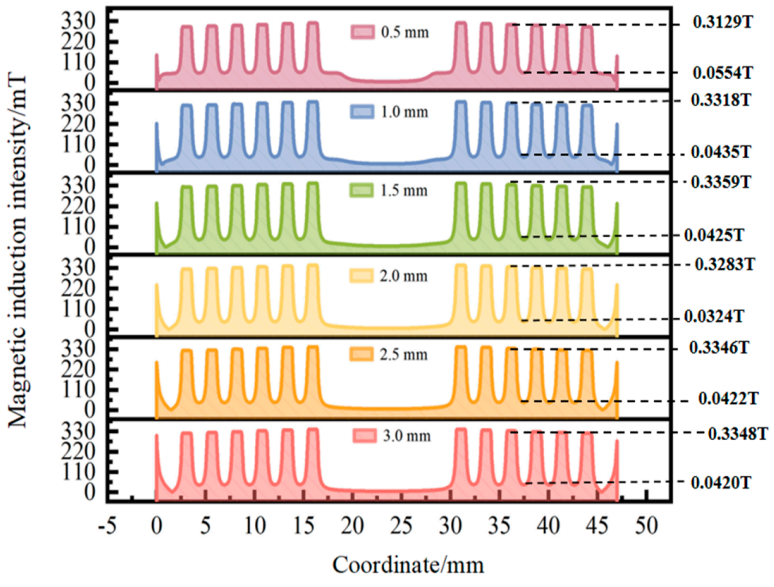

Figure 18. Magnetic induction intensity of the truncated line under different pole tooth heights.

5.5. Influence of Pole Tooth Width on Sealing Pressure

Setting the seal gap at 0.1 mm, with six pole teeth, a groove width of 1.5 mm, and a pole tooth height of 2.0 mm, the effect of pole tooth width on the performance of ferrofluid seals is studied. Widths ranging from 0.5 to 2.5 mm were selected, with a change gradient of 0.25 mm, to investigate the relationship between pole tooth width and ferrofluid seal pressure. The magnetic field maps of the sealing device under different pole tooth widths are shown in Figure 19.

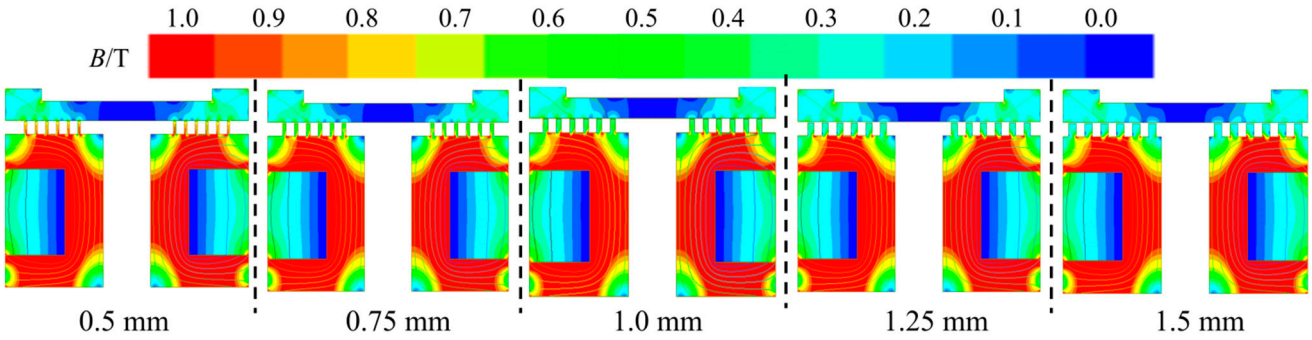

Figure 19. Magnetic field cloud image of a sealing device with different pole tooth widths.

Figure 20 shows Magnetic induction intensity of truncated line under different pole tooth widths. At a pole tooth width of 0.25 mm, the measured magnetic induction intensity on the pole tooth is significantly higher. As the pole tooth width increases, the magnetizing effect on the pole decreases, resulting in a reduction in magnetic induction intensity in certain areas of the pole tooth. Through quantitative analyses of the magnetic induction intensity distribution curve at the seal gap position, an increase in pole tooth width leads to a rapid decrease in the peak positive value of magnetic induction intensity. At pole tooth widths of 0.5 mm and 1.5 mm, the peak positive values of magnetic induction intensity are 0.4971 T and 0.2525 T, respectively. Increasing the pole tooth width by 1 mm reduces the peak positive value by a factor of 2. Although the negative peak value of magnetic induction intensity is closer to zero for large pole tooth widths, its variation can be approximately neglected compared to the variation in positive peak values. The sealing ability for pole tooth widths of 0.5, 0.75, 1.0, 1.25, and 1.5 mm was calculated using the pressure resistance formula, resulting in 52.13, 42.16, 35.53, 30.23, and 26.52 kPa, respectively. The rate of decline in sealing ability is relatively rapid. Among all parameters, the pole tooth width has a significant impact on sealing performance, second only to the seal gap's influence on sealing performance.

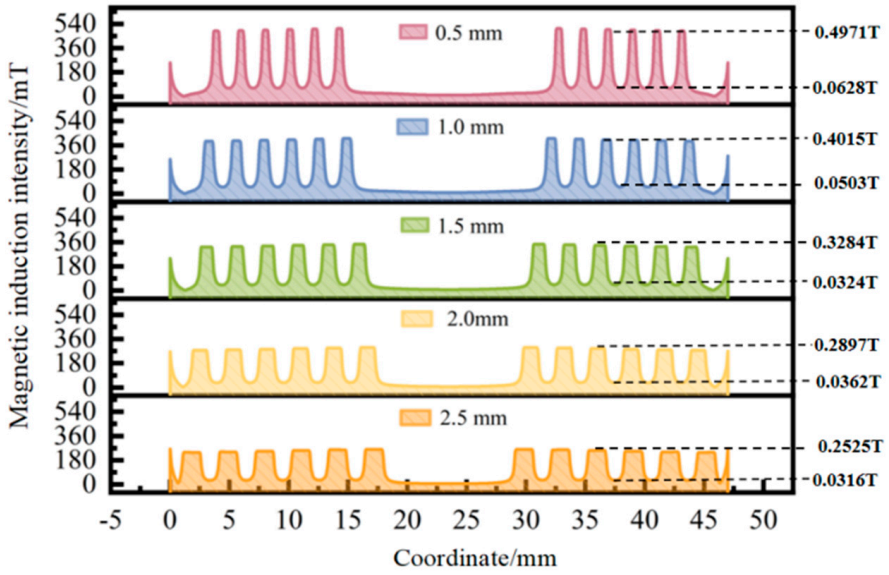

Figure 20. Magnetic induction intensity of truncated line under different pole tooth widths.

6. Test Verification

According to the safety valve technical specification "GB12241-2021" for the allowable deviation of the set pressure of a spring-loaded safety valve [29], when the set pressure is ≥0.5 MPa, a 3% deviation in the set pressure is allowed Figure 21 shows the test bench for the ferrofluid seal device of the safety valve. In the experiment, the coil of the electromagnet

was set to 10 turns, and the excitation current was 200 mA. The pressurized gas used was nitrogen, and six sets of experiments were conducted. The test results indicate that the sealing device failed at nitrogen pressures of 1.128, 1.125, 1.125, 1.128, 1.125, and 1.125 MPa.

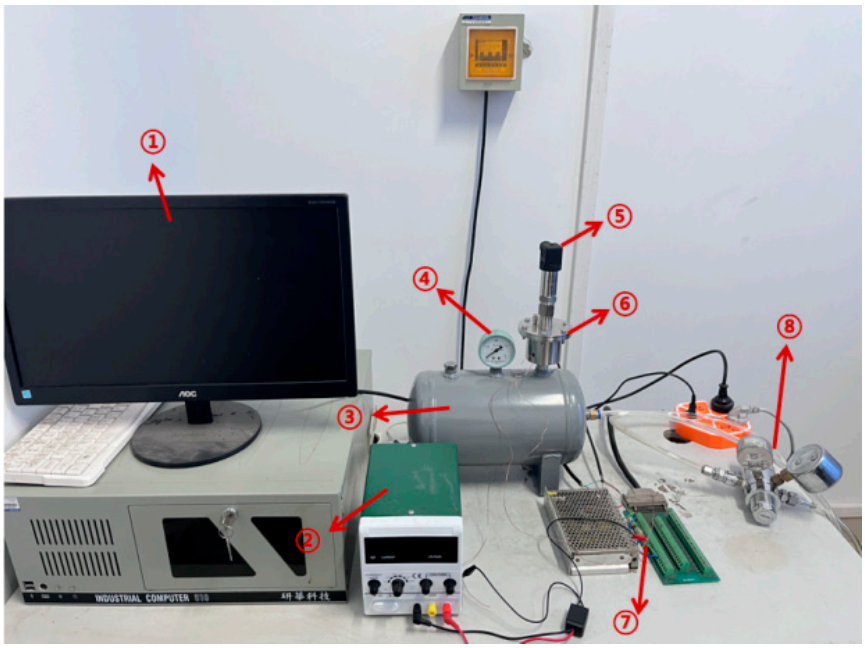

Figure 21. Test site diagram (① data acquisition computer; ②—DC power supply; ③—gas storage tank; ④—pressure gauge; ⑤—pressure sensor; ⑥—magnetic fluid seal safety valve; ⑦—data collection card; ⑧—pressure reducing valve).

Following the technical standard, to ensure seal safety, the reference limit pressure for the seal device was taken as 1.125 MPa. The allowable deviation value for this seal device was calculated to be ±0.034 MPa. The actual deviation value was found to be 0.003 MPa (1.128–1.125 MPa), which is significantly lower than the allowable deviation value. Thus, it can be concluded that the designed ferrofluid seal safety valve exhibits stability at the set pressure.

Upon energizing the DC power supply and inputting current, the ferrofluid is attracted to the gap of the sealing device, forming an "O"-type seal ring [30]. Once the pressure of the medium exceeds the pressure that the seal ring can withstand, the seal ring breaks, causing the valve to open and release the medium, thereby reducing the system pressure. Under the influence of the magnetic force, the valve disc quickly resets to close, re-establishing a stable "O"-type seal ring. As the sealing method of the safety valve combines mechanical sealing with ferrofluid sealing, this study focused on verifying the ferrofluid seal part, hence the removal of the spring part from the device during the experiment.

Figure 22 shows the relationship between the measured seal performance and the excitation current and number of coil turns in the experiment. Initially, with a fixed number of turns of 30, the excitation current increased linearly from 40 mA to 240 mA in increments of 20 mA, resulting in a linear improvement in the seal performance. When the excitation current reached 240 mA, the seal pressure was 61.22 kPa. Subsequently, by fixing the excitation current at 200 mA, the number of coil turns of the device varied linearly from 10 turns to 80 turns, showing a linear relationship between the seal pressure and the number of coil turns. Both results indicate that the seal performance improves linearly with the increase in magnetic field intensity, consistent with theoretical predictions regarding the seal pressure of the ferrofluid seal device, thus confirming the feasibility of this structure.

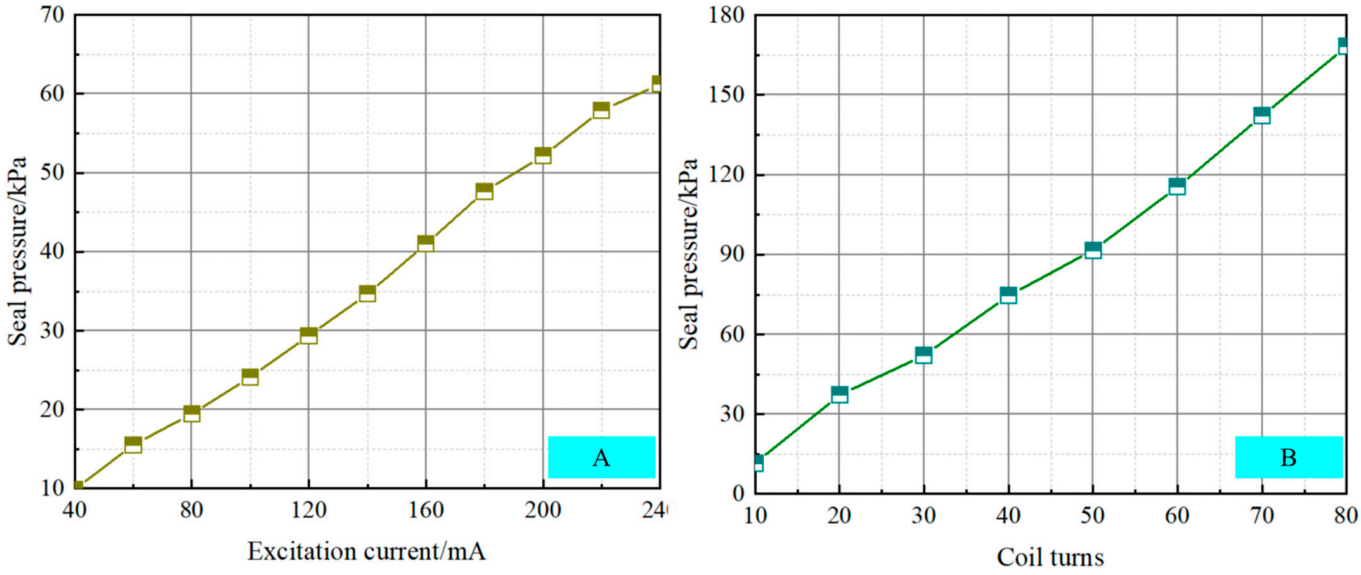

Figure 22. Experimental correlation parameter ((**A**) relation between sealing performance and excitation current; (**B**) relation between sealing performance and coil turns).

7. Conclusions

The study designed and systematically assessed a ferrofluid seal device for use in a safety valve, resulting in some important conclusions that provide preliminary validations of the feasibility of using a ferrofluid seal for safety valves. By conducting simulation calculations on the magnetic circuit, the study analyzed the impacts of key parameters of the device on the sealing capability, and further validated these through experiments, yielding specific conclusions, as follows:

(1) The study combined ferrofluid sealing with mechanical end-face sealing and designed a new type of seal structure for the safety valve. This structure enhances the stability and reliability of the safety valve seal device performance by applying ferrofluid without altering the system of the sealing device;

(2) Using numerical methods, the study investigated the effects of seal clearance, pole tooth height, pole tooth width, groove width, and number of seals on the performance of the magnetic fluid seal. The sealing capacity decreased rapidly with an increase in seal clearance. The trend shows an initial increase followed by a decrease with an increase in pole tooth length, a significant decrease with an increase in pole tooth width, an initial increase followed by a decrease with an increase in groove width, and an initial increase followed by a decrease with an increase in the number of seals. The optimal seal structural dimensions identified were a seal gap of 0.1 mm, a pole tooth height of 2.0 mm, a pole tooth width of 0.5 mm, a groove width of 1.5 mm, and six seals;

Variable	Sealing Performance	
Seal clearance	↑	↓
Pole tooth height	↑	↑↓
Pole tooth width	↑	↑
Groove width	↑	↑↓
Number of seals	↑	↑↓

(3) A novel ferrofluid seal safety valve device was designed as the main mechanical seal, augmented by the magnetic fluid seal as a compensatory seal. This design addresses the shortcomings of traditional spring-loaded safety valves by mitigating leakage issues and ensuring faster opening and closing. Testing conducted based on the manufactured ferrofluid safety valve device demonstrated stable set pressure capability and "zero leakage" features (the leakage rate of the sealed medium was

undetectable using the standard helium mass spectrometry method, with a limit of 1×10^{-11} (Pa·m^3)/s). The pressure resistance of the ferrofluid seal increases with a rise in excitation current and the number of coil turns. At an excitation current of 240 mA and 50 coil turns, the pressure resistance was 61.22 kPa, while at an excitation current of 200 mA and 80 coil turns, the pressure resistance reached 168.24 kPa.

Author Contributions: Conceptualization, Z.L. and Z.W.; methodology, W.L.; software, Y.J.; validation, C.S.; formal analysis, C.C.; investigation, C.S.; resources, J.M. and W.L.; data curation, Y.L.; writing—original draft preparation, Z.L.; writing—review and editing, Z.L.; visualization, W.L.; supervision, W.L.; project administration, W.L.; funding acquisition, Z.L. All authors have read and agreed to the published version of the manuscript.

Funding: This study was supported by the National Natural Science Foundation of China [52379092], "Kunlun Talents" Research Project [2023-QLGKLYCZX-032], Chengdu Science, Technology Bureau project [2024-YF09-0003-GX], Jiangsu South-to-North water transfer technology research and development project [JSNSBD202403], and Project funded by Changjiang Power Co., Ltd. [2324020007].

Data Availability Statement: Data can be obtained by mail from corresponding authors.

Conflicts of Interest: Authors Ziyue Wang and Changrong Shen were employed by the company Jiangsu Water Resources Co., Ltd. Author Ziyue Wang was employed by the company Sichuan Huadian Luding Hydropower Co., Ltd. Authors Chuanshi Cheng, Jie Min and Yuanyuan Li was employed by the company China Yangtze Power Co., Ltd. The remaining authors declare that the research was conducted in the absence of any commercial or financial relationships that could be construed as a potential conflict of interest.

References

1. Pan, S.; Wang, J.; Zhao, X.; Ren, C.; Xin, Y.; Wang, Z. New design and transient flow analysis of a claw vacuum pump with novel gear-claw rotors. *Vacuum* **2023**, *216*, 112470. [CrossRef]
2. Pan, S.; Wang, J.; Tan, Q.; Zhao, F.; Cui, D.; Zhang, C. Analysis and numerical simulation of claw vacuum pumps with novel three-claw rotors. *Vacuum* **2021**, *192*, 110442. [CrossRef]
3. Zhu, S.C.; Guo, J.X.; Zhao, L.F.; Li, H.H.; Zhu, F. Reliability Analysis of Seal Performance of Pressure vessel safety Valve. *China Spec. Equip. Saf.* **2008**, *24*, 68–69.
4. Fan, D. *The Study of Magnetoviscous Effects in High and Low Temperature*; Beijing Jiaotong University: Beijing, China, 2012.
5. Chen, F.; Zhang, J.; Li, Z.; Yan, S.; Li, W.; Yan, Z.; Liu, X. Effect of the surface coating of carbonyl iron particles on the dispersion stability of magnetorheological fluid. *Sci. Rep.* **2024**, *14*, 11358. [CrossRef] [PubMed]
6. Li, W.; Li, Z.; Qin, Z.; Yan, S.; Wang, Z.; Peng, S. Influence of the solution pH on the design of a hydro-mechanical magneto-hydraulic sealing device. *Eng. Fail. Anal.* **2022**, *135*, 106091. [CrossRef]
7. Li, W.; Li, Z.; Han, W.; Li, Y.; Yan, S.; Zhao, Q.; Gu, Z. Pumping-velocity variation mechanisms of a ferrofluid micropump and structural optimization for reflow inhibition. *Phys. Fluids* **2023**, *35*, 052005.
8. Chen, F.; Zhang, J.; Guo, Q.; Liu, Y.; Liu, X.; Ding, W.; Yan, S.; Yan, Z.; Li, Z. Carbonyl Iron Particles' Enhanced Coating Effect Improves Magnetorheological Fluid's Dispersion Stability. *Materials* **2024**, *17*, 4449. [CrossRef]
9. Philipse, A.P.; Maas, D. Magnetic colloids from magnetotactic bacteria: Chain formation and colloidal stability. *Langmuir* **2002**, *18*, 9977–9984. [CrossRef]
10. Li, W.; Li, Z.; Han, W.; Li, Y.; Yan, S.; Zhao, Q.; Chen, F. Measured viscosity characteristics of Fe_3O_4 ferrofluid in magnetic and thermal fields. *Phys. Fluids* **2023**, *35*, 012002. [CrossRef]
11. Li, W.; Li, Z.; Han, W.; Tan, S.; Yan, S.; Wang, D.; Yang, S. Time-mean equation and multi-field coupling numerical method for low-Reynolds-number turbulent flow in ferrofluid. *Phys. Fluids* **2023**, *35*, 125145. [CrossRef]
12. Li, Z.; Qing, J.; Shen, C.; Ma, S.; Wu, D.; Zhu, G.; Wang, Y.; Yang, C.; He, X.; Su, J. Study on performance optimization of double screw-magnetic fluid combination seal. *Phys. Fluids* **2024**, *36*, 022021. [CrossRef]
13. Yang, X.; Li, D.; He, X.; Zhang, H. Numerical and Experimental Studies of Alternative Combined Magnetic Fluid and Labyrinth Seal with Large Gap. *J. Mech. Eng.* **2014**, *50*, 175–179. [CrossRef]
14. Wang, Z.S. *Theoretical and Experimental Research of Mechanical—Magnetic Fluid Combined Seal*; Beijing Jiaotong University: Beijing, China, 2016.
15. Li, W.; Li, Z.; Wang, Z.; Wu, F.; Xu, L.; Peng, S. Turbulence intensity characteristics of a magnetoliquid seal interface in a liquid environment. *Coatings* **2021**, *11*, 1333. [CrossRef]
16. Liu, T.; Cheng, Y.; Yang, Z. Design optimization of seal structure for sealing liquid by magnetic fluids. *J. Magn. Magn. Mater.* **2005**, *289*, 411–414. [CrossRef]

17. Petcharoen, K.; Sirivat, A. Synthesis and characterization of magnetite nanoparticles via the chemical co-precipitation method. *Mater. Sci. Eng. B* **2012**, *177*, 421–427. [CrossRef]
18. Wang, Y.M.; Cao, X.; Liu, G.H.; Hong, R.Y.; Chen, Y.M.; Chen, X.F.; Li, H.Z.; Xu, B.; Wei, D.G. Synthesis of Fe_3O_4 magnetic fluid used for magnetic resonance imaging and hyperthermia. *J. Magn. Magn. Mater.* **2011**, *323*, 2953–2959. [CrossRef]
19. Tsai, C.S.; Chen, H.Y.; Chang, K.P. Using chemical coprecipitation method to prepare magnetite magnetic fluids and explore its applications in hyperthermia. *Key Eng. Mater.* **2011**, *474*, 1776–1780. [CrossRef]
20. Li, Z.; Li, W.; Wang, Q.; Xiang, R.; Cheng, J.; Han, W.; Yan, Z. Effects of medium fluid cavitation on fluctuation characteristics of magnetic fluid seal interface in agricultural centrifugal pump. *Int. J. Agric. Biol. Eng.* **2021**, *14*, 85–92. [CrossRef]
21. Agnihotri, P.; Lad, V.N. Magnetic nanofluid: Synthesis and characterization. *Chem. Pap.* **2020**, *74*, 3089–3100. [CrossRef]
22. Xu, L.F. *Preparation and Characterization of Fe_3O_4@SiO_2 Silicon Oil Based Magnetic Fluid*; Beijing Jiaotong University: Beijing, China, 2017.
23. Liang, A.; Li, H.; Zhang, W.; Yao, Z.; Zhu, B.; Wang, F. Study on pressure fluctuation and rotating stall characteristics in the vaneless space of a pump-turbine in pump mode. *J. Energy Storage* **2024**, *94*, 112385. [CrossRef]
24. Hu, L.; Liang, A.; Li, H.; Zhang, W.; Zhu, B. Impact of rotor-stator axial spacing on the gas-liquid-solid flow characteristics of a multiphase rotodynamic pump based on the Euler multi-fluid model. *Phys. Fluids* **2024**, *36*, 063314. [CrossRef]
25. Li, H.; Yang, J.; Zhang, W.; Hu, L.; Liang, A.; Yao, Z. Energy performance and unsteady gas-liquid flow characteristics of a multiphase rotodynamic pump: An experiment. *Appl. Energy* **2024**, *375*, 124112. [CrossRef]
26. Xu, L.; Kan, K.; Zheng, Y.; Liu, D.; Binama, M.; Xu, Z.; Yan, X.; Guo, M.; Chen, H. Rotating Stall Mechanism of Pump-Turbine in Hump Region: An Insight into Vortex Evolution. *Energy* **2024**, *292*, 130579. [CrossRef]
27. Liu, D.; Li, Z.; Xu, L.; Li, J.; Yang, Y.; Wang, X.; Pang, J.; Liu, X. Vortex Motion in Vaneless Space and Runner Passage of Pump-Turbine in S-Shaped Region. *Phys. Fluids* **2024**, *36*, 025115. [CrossRef]
28. Ren, Z.; Li, D.; Zhou, W.; Li, Z.; Wang, H.; Liu, J.; Li, Y.; Khoo, B.C. Gas–liquid mass-transfer characteristics during dissolution and evolution in quasi-static and dynamic processes. *Int. J. Multiph. Flow* **2024**, *180*, 104970. [CrossRef]
29. *GB/T 12241-2021*; " Safety Valves—General Requirements" Standard. State Administration for Market Regulation, Standardization Administration of China: Beijing, China, 2021.
30. Li, W.; Li, Z.; Han, W.; Li, D.; Yan, S.; Zhou, J. Study of The Flow Characteristics of Pumped Media in The Confined Morphology of A Ferrofluid Pump with Annular Microscale Constraints. *J. Fluids Eng.* **2024**, 1–31. [CrossRef]